coatings

MDPI

Article

Solution-Processed Mg-Substituted ZnO Thin Films for Metal-Semiconductor-Metal Visible-Blind Photodetectors

Chien-Yie Tsay *, Shih-Ting Chen and Man-Ting Fan

Department of Materials Science and Engineering, Feng Chia University, Taichung 40724, Taiwan; sarah15937@gmail.com (S.-T.C.); wendy5252065@gmail.com (M.-T.F.)

* Correspondence: cytsay@mail.fcu.edu.tw; Tel.: +886-4-2451-7250 (ext. 5312)

Received: 22 March 2019; Accepted: 22 April 2019; Published: 25 April 2019

Abstract: The effects of Mg on the microstructural, optical, and electrical properties of sol-gel derived ZnO transparent semiconductor thin films and the photoelectrical properties of photodetectors based on $Mg_xZn_{1-x}O$ (where x = 0 to 0.3) thin films with the metal-semiconductor-metal (MSM) configuration were investigated in this study. All the as-synthesized ZnO-based thin films had a single-phase wurtzite structure and showed high average transmittance of 91% in the visible wavelength region. The optical bandgap of $Mg_xZn_{1-x}O$ thin films increased from 3.25 to 3.56 eV and the electrical resistivity of the films rose from 6.1×10^2 to 1.4×10^4 Ω·cm with an increase in Mg content from x = 0 to x = 0.3. Compared with those of the pure ZnO thin film, the PL emission peaks of the MgZnO thin films showed an apparent blue-shift feature in the UV and visible regions. The photo-detection capability was investigated under visible, UVA, and UVC light illumination. Linear *I-V* characteristics were obtained in these ZnO-based photodetectors under dark and light illumination conditions, indicating an ohmic contact between the Au electrodes and ZnO-based thin films. It was found that the pure ZnO photodetector exhibited the best photoconductivity gain, percentage of sensitivity, and responsivity under UVA illumination. Under UVC illumination, the photoconductivity gain and percentage of sensitivity of the MgZnO photodetectors were better than those of the pure ZnO photodetector.

Keywords: transparent oxide semiconductor; MgZnO thin film; solution process; visible-blind photodetector; photoconductivity; responsivity

1. Introduction

Solid-state photodetectors based on wide bandgap semiconductors, such as GaN, ZnO, SiC, and Diamond, are especially attractive for ultraviolet (UV) radiation detection. Their investigation and development open up potential applications in fields as varied as environmental protection, medicine and healthcare, space communication and exploration, optoelectronic circuits, and military surveillance [1–3]. It is general knowledge that when a semiconductor material is exposed to solar radiation, the photon energy creates electron-hole pairs inside the material, and the charges can be subsequently collected to produce electrical signals. The tailoring of optical properties (especially the bandgap energy) of crystalline semiconductor materials could lead to a broad-spectral response of detection for photodetectors and expand their application fields [4].

ZnO is an *n*-type II-VI group semiconductor with a direct wide bandgap (~3.37 eV) and exhibits a wide range of electrical tenability. Its thermal, chemical, and mechanical stability at room temperature make it attractive for use in electronics, optoelectronics, and renewable energy generation [5,6]. The carriers of ZnO semiconductor thin films, originating from oxygen vacancies and zinc interstitials,

can be adjusted by doping or substituting impurities (metal elements) to meet the device operating requirements [7–9]. The replacement of Zn^{2+} ions in the ZnO lattice by Mg^{2+} ions can take place due to the electronegativity difference between Mg^{2+} (1.35) and Zn^{2+} (1.65) ions [10]. The optical bandgap of Mg-substituted ZnO ($Mg_xZn_{1-x}O$) semiconductor thin films can be significantly tuned from 3.37 to 7.8 eV by varying the Mg composition to make them feasible for use as solar-blind or visible-blind UV photodetectors with different cutoff wavelengths [11,12]. Such a feature suggests that MgZnO semiconductors have been extensively researched and are among the most promising photoelectrical materials for broadband UV photodetector application. Liu et al. have demonstrated that the light sensitivity of sol-gel derived $Mg_{0.2}Zn_{0.8}O$ MSM photodetectors on quartz substrate ranges from near UV to deep UV [13]. The UV photodetector based on sol-gel synthesized $Mg_{0.18}Zn_{0.82}O$ nanoparticle has been fabricated with the UV/visible reject ratio up to two orders of magnitude and the peak response at 322 nm [14]. Rana et al. fabricated multilayer MgZnO/ZnO thin films for the UV photodetector. They showed that the $Mg_{0.02}Zn_{0.98}O$/ZnO photodetector had the highest responsivity under exposure to UV light (365 nm) at 5 V bias [15].

Various vacuum deposition methods, such as radio frequency magnetron sputtering and pulsed laser deposition, are generally considered for producing high-quality functional oxide thin films [16–19]. Recently, chemical solution approaches for depositing metal oxide thin films have inspired novel research because they have several advantages over vacuum deposition techniques, such as a simple processing setup, cost-effectiveness, easy large-area thin film deposition, high film growth rate, and excellent compositional control of dopants in the metal oxide thin films [20,21]. Photodetectors made with solution-processed metal oxide semiconductors, which combine desirable manufacturing advantages and state-of-the-art performance metrics, have progressed extremely well and emerged as candidates for next-generation light sensing or driving devices [22]. Compared with photovoltaic detectors, photoconductive detectors are limited by a longer response time, higher dark current, and smaller signal-to-noise ratio. However, photoconductive detectors continue to attract interest because of their high photoconductive gain, better linearity, fabrication simplicity, and capability for integration with other optoelectronic devices [17,23].

In the current work, wide bandgap $Mg_xZn_{1-x}O$ (x = 0 to 0.3) semiconductor thin films were deposited onto alkali-free glass substrates by a sol-gel spin-coating process. The effects of incorporating Mg into ZnO thin films on the structural features, surface morphology, and optical, electrical, photoluminescence, and photoelectrical properties were extensively investigated. In addition, metal-semiconductor-metal (MSM) photodetectors were fabricated by depositing Au electrodes on $Mg_xZn_{1-x}O$ thin films, and their ability to detect UV radiation as visible-blind photodetectors was evaluated. Most of the previous research focused on the study of the structural and optical properties of MgZnO thin films and the responsivity of MgZnO photodetectors. In this study, the authors not only investigated the role of Mg content on the structural features and optical parameters of the sol-gel derived ZnO thin films but also reported the electrical properties of the MgZnO thin films and important photoconductive properties of the MgZnO photodetectors for proving more understanding in visible-blind photodetectors.

2. Materials and Methods

Mg-substituting ZnO ($Mg_xZn_{1-x}O$, where x = 0, 0.1, 0.2, and 0.3) thin films were deposited on alkali-free glasses (NEG OA-10, dimensions of 50 × 50 × 0.7 mm^3) by sol-gel method and spin coating technique. Analytical grade zinc acetate dihydrate and magnesium nitrate hexahydrate were dissolved in 2-methoxyethanol (2-ME) and diethanolamine (DEA) solution. The concentration of metal ions in the resultant solution was 0.5 mol/L, and the molar ratio of DEA to metal ions was kept at 1.0. Each mixture was stirred with a magnetic stirrer at 60 °C for 2 h on a hotplate until it became clear and homogeneous. After that, the solutions were aged at room temperature for 120 h before being used as the coating precursor solutions. These $Mg_xZn_{1-x}O$ sol-gel films were spin-coated onto pre-cleaned glass substrates at a speed of 1500 rpm for 30 s, followed by heating at 300 °C for 10 min to evaporate the solvents and

remove the organics. This procedure was performed three times, and then the resulting dried sol-gel films were annealed in a quartz tube furnace at 500 °C for 1 h in air to burn out residual organic matter and form crystalline oxide thin films.

The crystal structure, crystallite orientation, and crystallinity of as-prepared $Mg_xZn_{1-x}O$ thin films were determined using an X-ray diffractometer (D8 SSS, Bruker, Billerica, MA, USA) with Cu-Kα radiation (λ = 1.5406 Å) by glancing incidence technique at an incident angle of 0.8° and 2θ range from 25° to 65°. The microstructural features of the films were investigated using a field-emission scanning electron microscope (FE-SEM, S-4800, Hitachi High-Technology, Tokyo, Japan); the surface morphology and surface roughness of the films were characterized by tapping-mode scanning probe microscope (SPM, NS4/D3100CL/MultiMode, Digital Instruments, Mannheim, Germany) on a scan area of 500 × 500 nm^2. For characterizing the light transport ability, the optical transmittance and reflection spectra of the glass/$Mg_xZn_{1-x}O$ thin film samples were recorded using an ultraviolet-visible (UV-Vis) spectrophotometer (U-2900, Hitachi High-Technology, Tokyo, Japan). The room-temperature emission spectra of four ZnO-based thin films were recorded by photoluminescence (PL) spectrometer (LabRAM HR, HORIBA Jobin Yvon, Paris, France) using an excitation light source of 325-nm He-Cd laser. The electrical characteristics of the thin film samples were measured by a Hall effect measurement system (HMS-3000, Ecopia, Gyeonggi-do, Korea) using the van der Pauw configuration under a 0.55 T magnetic field.

Photodetectors based on the metal-semiconductor-metal (MSM) configuration were fabricated by patterning Au interdigitated electrodes (80 nm thick) onto the surfaces of oxide films with a stainless steel shadow mask by E-gun evaporation; a schematic of the designed Au−$Mg_xZn_{1-x}O$ photodetector is illustrated in Figure 1. Each electrode had six fingers; the electrode fingers were 2900 μm long and 100 μm wide with a 150 μm spacing gap (Figure S1). Au interdigitated electrodes were employed to collect the photo-generated carriers. The current–voltage (*I*–*V*) characteristics and the time-dependent photoresponse of the photodetectors were measured using a Source-Measure Unit (Jiehan 5000, Taichung, Taiwan) in the dark state or under illumination of visible, UVA, and UVC light. The incident power densities, produced from mercury lamps, measured on the surface of a thin film sample were 1.84, 2.14, and 5.74 mW/cm^2 for visible, UVA, and UVC radiation, respectively. Before the photocurrent and photoswitching characteristics were measured under light illumination, each photodetector was kept in a black box for 12 h to eliminate any trapped charges. The experimental results were confirmed by repeating the examinations and measurements.

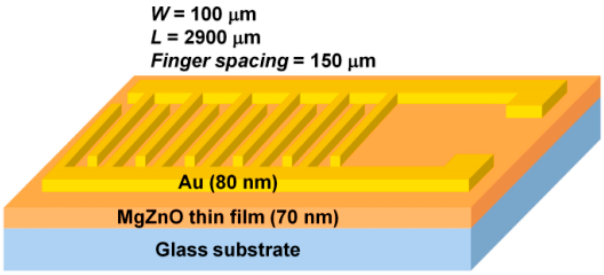

Figure 1. Schematic of designed Au−$Mg_xZn_{1-x}O$ photodetector on glass substrate with metal-semiconductor-metal (MSM) structure.

3. Results and Discussion

XRD patterns of sol-gel derived Mg-substituted ZnO ($Mg_xZn_{1-x}O$, where x = 0 to 0.3) thin films on glass substrates are shown in Figure 2. Six diffraction peaks were identified by comparison with the Joint Committee for Powder Diffraction Standards (JCPDS) card No. 036-1451 for corresponding to the (100), (002), (101), (102), (110), and (103) crystallographic planes of ZnO crystal. In addition, no diffraction peaks corresponding to the secondary phase, such as MgO, were detected implying that the Mg^{2+} was well incorporated into the ZnO lattice. Results of XRD examination indicated that

these as-synthesized metal oxide thin films were polycrystalline in nature, confirming the formation of a single-phase hexagonal wurtzite structure. Analysis of XRD data revealed that the full widths at half-maximum (FWHMs) for the three major diffraction peaks, (100), (002), and (101), increased with increasing Mg content, which indicated that the substitution of Mg in the ZnO thin films could reduce the crystallite size. The average crystallite size was determined from the FWHMs of (100), (002), and (101) peaks of each $Mg_xZn_{1-x}O$ thin film using Scherrer's formula and is presented in Table 1. Calculated results showed that when the Mg content increased from $x = 0$ to $x = 0.3$, the average crystallite size decreased from 18.3 to 13.0 nm. That reduction revealed that the incorporation of Mg into ZnO crystal could retard grain growth and produce oxide films consisting of a fine-grained microstructure. That fact was also verified by FE-SEM observation of $Mg_xZn_{1-x}O$ thin films, as shown in Figure 3.

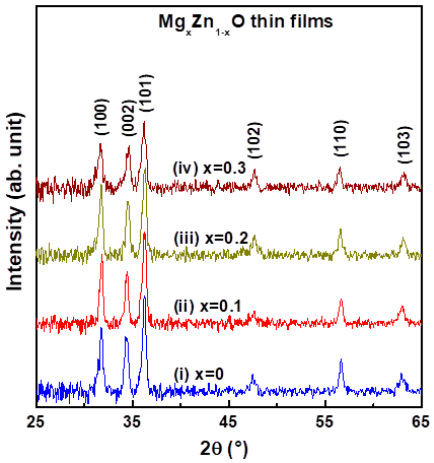

Figure 2. X-ray diffraction (XRD) patterns of sol-gel derived $Mg_xZn_{1-x}O$ thin films with different Mg contents on glass substrates.

Table 1. Structural features and optical properties of sol-gel derived $Mg_xZn_{1-x}O$ thin films.

Mg Content	Average Crystallite Size (nm)	Root Mean Square (RMS) Roughness (nm)	Average Transmittance (%) [a]	Average Reflectance (%) [b]	Optical Bandgap (eV)	Urbach Energy (meV)
$x = 0$	18.3	5.9	91.3	9.45	3.25	117
$x = 0.1$	16.7	4.2	92.4	8.20	3.41	136
$x = 0.2$	14.7	3.7	92.3	8.50	3.55	172
$x = 0.3$	13.0	3.5	93.2	6.88	3.65	206

The average transmittance values [a] and average reflectance values [b] were calculated from the transmittance and reflectance data of wavelengths from 400 to 800 nm.

It is well known that the diffraction peak broadening of polycrystalline metal oxide thin films is associated not only with crystallite size reduction but also lattice strain induced in the thin films [24]. While the ionic radii of the dopant Mg^{2+} (0.057 nm) is relatively smaller than that of the host Zn^{2+} (0.060 nm), some Zn^{2+} ions in the crystal lattice of the host oxide material were easily replaced by Mg^{2+} ions (>30 at.%) without changing the crystal structure, proving the possibility of MgZnO solid solution formation [25,26]. The substitution of Mg^{2+} ions for Zn^{2+} ions slightly distorted the lattice of the ZnO crystal. Such lattice distortion may facilitate the formation of ZnO crystal nuclei and inhibit grain growth, leading to the obtained MgZnO thin films having a microstructure finer than that pure ZnO thin film. In addition, a slight shift of the (100) peak toward a lower diffraction angle region and the (002) peak toward a higher diffraction angle region were found with an increase in Mg content, indicating changes in the lattice parameters (a-axis and c-axis lengths) after Mg was incorporated into ZnO crystals [19,27].

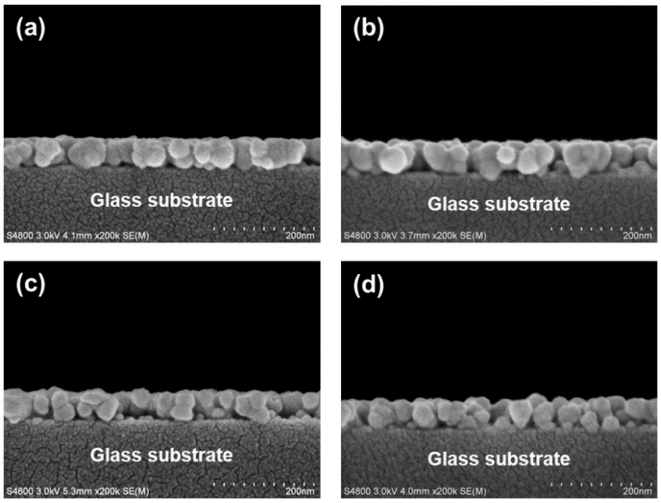

Figure 3. Cross-sectional field-emission scanning electron microscope (FE-SEM) micrographs of $Mg_xZn_{1-x}O$ thin films on glass substrates: (**a**) $x = 0$, (**b**) $x = 0.1$, (**c**) $x = 0.2$, and (**d**) $x = 0.3$.

Figure 3 shows cross-sectional FE-SEM micrographs of sol-gel derived $Mg_xZn_{1-x}O$ thin films on glass substrates. The film thickness of each oxide thin film sample was estimated from the corresponding FE-SEM micrograph. The mean film thicknesses of the ZnO (Figure 3a) and MgZnO (Figure 3b–d) thin films were 72 and 70 nm, respectively. As can be seen from the FE-SEM micrographs, these obtained ZnO-based thin films had a significantly granular microstructure, and nano-sized pores formed inside the polycrystalline oxide thin films. Kim et al. reported that the formation of nano-sized pores inside the sol-gel derived ZnO-based thin films were related to the thermal decomposition of the precursors and residual organics in dried sol-gel films [28]. The presence of nano-sized pores is one of the major reasons why the electrical properties of solution-processed oxide semiconductor thin films are inferior to the sputtered oxide semiconductor thin films. However, the solution-processed oxide thin films exhibited a porous microstructure and had relatively large grain boundary areas, which could make them applicable as the sensing layer in sensors and detectors [6]. In addition, it can be clearly seen in Figure 3 that the particle sizes were significantly affected by the Mg content. The plane-view FE-SEM micrographs showed a similar microstructural feature with the cross-sectional FE-SEM micrographs (Figure S2). The average grain sizes of the $Mg_xZn_{1-x}O$ thin films, as determined from plane-view FE-SEM micrographs, were 43.4, 42.0, 38.9, and 37.6 nm for $x = 0$, $x = 0.1$, $x = 0.2$, and $x = 0.3$, respectively. The observation of the structural features of the films by FE-SEM was in good agreement with the XRD results.

Three-dimensional (3D) SPM images were taken from the free surface of each thin film sample for investigation of the surface morphology and surface roughness. SPM examination revealed that the ZnO-based thin films consisted of nano-sized particles and exhibited a crack-free surface; the mean particle size of the ZnO thin film was larger than that of the MgZnO thin films (Figure S3). Table 1 presents that the surface root mean square (RMS) decreased with increases in Mg content due to changes in particle size. This tendency of the microstructure, according to SPM examination, is consistent with the XRD examination and FE-SEM observation. The obtained oxide thin films exhibited a moderately flat surface morphology, which facilitates the creation of a uniform junction interface between an Au electrode and a ZnO-based semiconductor.

The optical properties of the functional oxide thin film in the visible and UV light regions are important factors in photodetector applications. Figure 4 depicts the optical transmittance spectra of the glass/$Mg_xZn_{1-x}O$ thin film samples in the wavelength range of 200–800 nm. Each transmittance spectrum exhibited high transparency (>91%) in the visible region and a steep absorption edge in the UV region. Moreover, the transmittance was almost zero when the wavelength was less than 250 nm. The average transmittances of the MgZnO thin films (>92.0%) were slightly higher than that of the

ZnO thin film (91.3%) in visible light of 400 to 800 nm due to a flatter surface and lower reflectance (Figure S4). The high visible light transmittance was due to weak absorption and a slight scattering of the obtained ZnO-based thin films, which make them suitable for application in transparent circuitry and invisible electronics. Plots of the first derivative of the transmittance (dT/dλ) versus wavelength are presented in the inset of Figure 4. The peak value for each curve provided a corresponding absorption band edge (cut-off wavelength) of the oxide films, the value of which significantly shifted towards the lower side with increasing Mg content, indicating blue-shift behavior. In addition, a tail−like bow was observed in the absorption edge region; this feature is related to the presence of structural defects such as grain boundaries and interstitial sites [17]. The comparatively low transmittance coefficient in the UV light region (Figure 4) was attributed to the high absorption rate because of the nature of the wide bandgap oxide semiconductor.

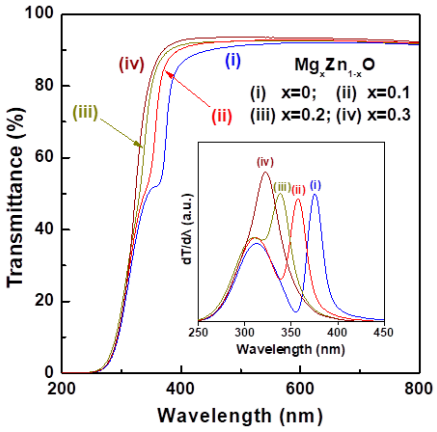

Figure 4. Optical transmission spectra of glass/$Mg_xZn_{1-x}O$ thin film samples. The inset shows the plots of dT/dλ versus wavelength of the corresponding thin film samples.

The data of the recorded transmittance spectrum allowed us to determine the optical bandgap energy (E_g) and Urbach energy (E_u) of the obtained $Mg_xZn_{1-x}O$ semiconductor thin films. The absorption coefficient (α) of the transparent thin films was calculated by using the following formula:

$$\alpha(\lambda) = 1/d \ln(1/T) \quad (1)$$

where d is the thickness of the thin film sample and T is the measured transmittance coefficient. The optical bandgap energy (E_g) of the semiconductor thin films was estimated by employing the Tauc relation (Equation (2)) [20]:

$$(\alpha h\nu)^n = B(h\nu - E_g) \quad (2)$$

where h is Planck's constant, ν is the frequency of incident light, $n = 2$ for direct bandgap material, and B is an energy-independent constant. The optical bandgap energy of each ZnO-based thin film was determined by extrapolation of the straight-line portion of the absorption curve to intercept the photon energy axis at $(\alpha h\nu)^2$ equal to zero from the plot of $(\alpha h\nu)^2$ versus photon energy (hν) (Figure 5a). Clearly, the optical bandgap energy, which was derived from the Tauc's plot, increased with the Mg composition from 3.25 eV for ZnO to 3.65 eV for $Mg_{0.3}Zn_{0.7}O$ (Table 1). Several research groups have reported that the blue-shift of the absorption edge and tailoring of the corresponding optical bandgap of the $Mg_xZn_{1-x}O$ thin films can be attributed to the incorporation of Mg ions into the ZnO lattice and is caused by the quantum confinement effect [25,29]. We confirmed that the optical bandgap of the $Mg_xZn_{1-x}O$ thin films could be tuned by changing the Mg content. The experimental results of optical bandgap engineering are in good accordance with the observations of Singh et al. [30] and Sonawane et al. [31].

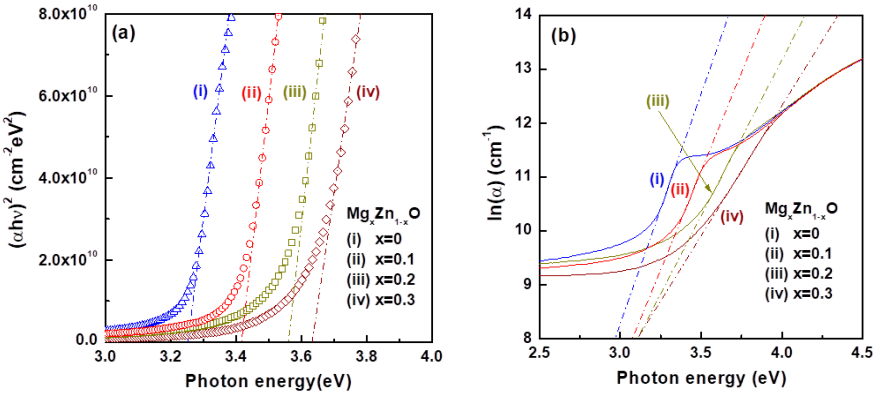

Figure 5. (**a**) Plot of $(\alpha h\nu)^2$ versus photon energy ($h\nu$) and (**b**) plot of ln(α) versus photon energy ($h\nu$) of $Mg_xZn_{1-x}O$ thin films.

Microstructural lattice disorder of the semiconductors caused by defect centers or carrier–impurity interactions could induce the formation of band tailing in the bandgap; this energy is associated with the Urbach tail, namely, Urbach energy. The relationship between absorption coefficient (α), photo energy ($h\nu$), and Urbach energy (E_u) can be expressed as follows [32]:

$$\alpha = \alpha_0 \exp(h\nu/E_u) \quad (3)$$

where α_0 is a constant. Figure 5b shows the plot of the variation of ln(α) with photo energy ($h\nu$). We determined the Urbach energy by calculating the inverse of the slope of the linear part of the absorption curve. The obtained Urbach energies were monotonically increased from 117 to 206 meV as the impurity content increased (Table 1).

Two emission signals were detected from the PL spectra for the solution processed $Mg_xZn_{1-x}O$ thin films (Figure 6). The sharp emission peak in the UV region (377−338 nm) corresponded to near-band-edge emission (NBE), which was attributed to radiative excitation recombination, and the other broad emission band in the visible region (620−550 nm) was attributed to the presence of deep-level defects due to native point defects and impurities in the oxide films [33,34]. The PL intensity of NBE emission was enlarged in the $x = 0.1$ and $x = 0.2$ samples, and the peak position of the NBE emission shifted toward the short wavelength region with increased Mg content. This trend of shifting is consistent with the absorption band edge of optical transmission spectra. Compared with those of the pure ZnO thin film, the PL emission peaks of the MgZnO thin films showed an apparent blue-shift in the UV and visible regions. The two methods (Tauc's plot and band-edge emission) yielded similar results. In addition, a significant observation from Figure 6 is that the intensity of the broad emission band increased considerably with increases in Mg content. The enhanced visible emissions can be ascribed to the recombination of electrons in the singly ionized oxygen vacancy center with photoexcited holes in the valence band [35]. The PL intensity ratio of UV peak to visible peak is related to the crystal quality of the oxide films. We found that the emission intensity ratio of the $Mg_{0.1}Zn_{0.9}O$ thin film was higher than that of the pure ZnO thin film, which can be attributed to decrease the defect concentration fraction and improved crystal quality [26].

The electrical properties, including the major carrier concentration and electrical resistivity, of the $Mg_xZn_{1-x}O$ thin films were examined by Hall effect measurement and are presented in Figure 7. Measurement results showed that these thin film samples exhibited n-type conductivity. The mean electron concentration (n) decreased from 4.64×10^{14} to 2.51×10^{13} cm^{-3} with increasing Mg content, and the mean resistivity (ρ) rose from 6.08×10^{2} to 8.68×10^{4} Ω·cm because the electrical resistivity of semiconductor materials is almost inversely proportional to the major carrier concentration. Substitution of Mg^{2+} for Zn^{2+} has no significant contribution to the cation charge in ZnO. Singh et al. demonstrated that the sol-gel synthesized MgZnO films with porosity attributing to relatively high

resistivity level [30]. Mg incorporated into ZnO crystals not only increased the grain boundary area to form electrical barriers and scattering of the carriers but also decreased the oxygen defects as the Mg–O bond has a more ionic character than the Zn–O bond that reduced the electron concentration and simultaneously increased in resistivity [15,20,36]. Cohen et al. have reported that increasing the Mg content from 0 to 20% could decrease the conductivity, mobility, and electron concentration in sputtered ZnO-based thin films [37]. Because the incorporation of Mg into ZnO led to an increase in the effective mass compared to ZnO.

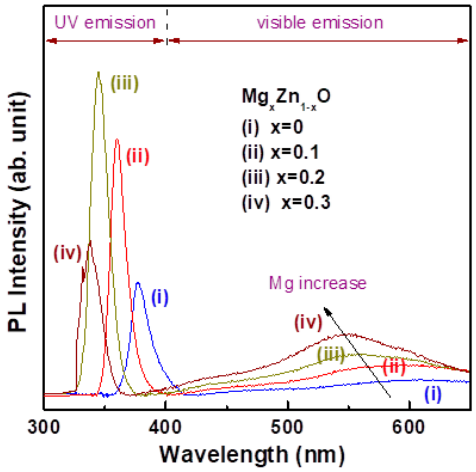

Figure 6. Room temperature photoluminescence (PL) spectra of nanocrystalline $Mg_xZn_{1-x}O$ thin films.

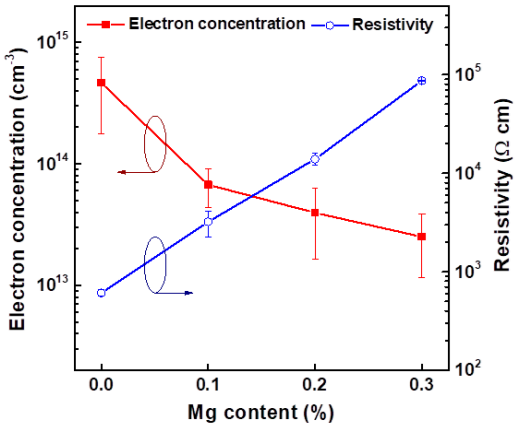

Figure 7. Variation in mean electron concentration (n) and mean resistivity (ρ) of nanocrystalline $Mg_xZn_{1-x}O$ thin films with Mg content.

The dependency of the photosensing ability under illumination of different wavelengths of light (visible light: $\lambda > 400$ nm, UVA light: $\lambda \approx 320–400$ nm, and UVC light: $\lambda \approx 200–280$ nm) were studied to examine the current–voltage (I–V) characteristic (Figure 8 and Figure S5) and switching characteristic (Figure 9). Dark currents and photocurrents of the sol-gel synthesized $Mg_xZn_{1-x}O$ thin films were measured between two Au electrodes when the photodetectors were irradiated with visible UVA, and a UVC light or without light illumination by varying the bias voltage from −5 V to +5 V across the semiconductor/electrode junctions. The current flow measured without light illumination was defined as dark current (I_{dark}). Under light illumination, carriers (electron−hole pairs) were generated in the photoactive materials (pure ZnO and MgZnO), enhancing current flow and achieving photoconductive properties.

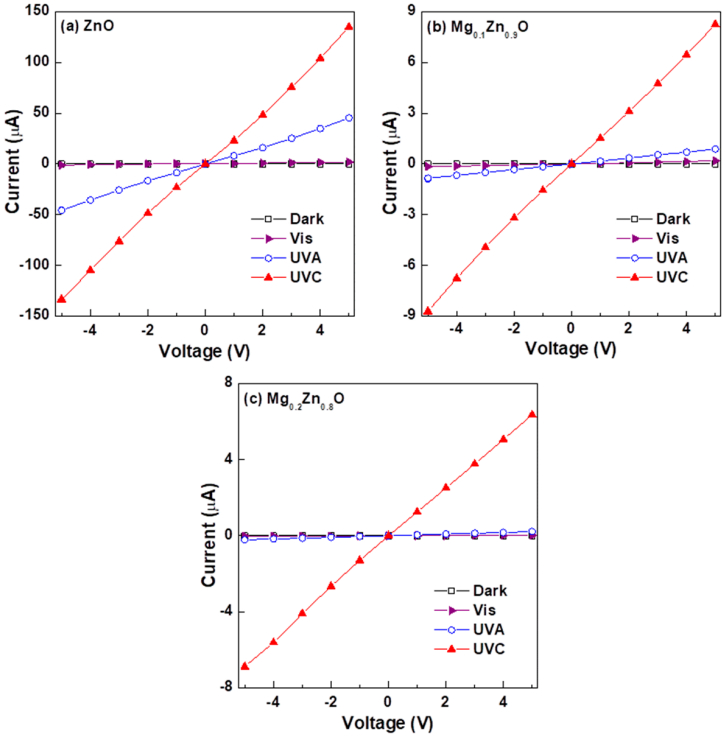

Figure 8. Current–voltage (*I*–*V*) characteristics of $Mg_xZn_{1-x}O$ photodetectors showing dark current and photoilluminated currents under irradiation with visible UVA and UVC light. The photodetectors were based on (**a**) ZnO, (**b**) $Mg_{0.1}Zn_{0.9}O$, and (**c**) $Mg_{0.2}Zn_{0.8}O$ semiconductor thin films.

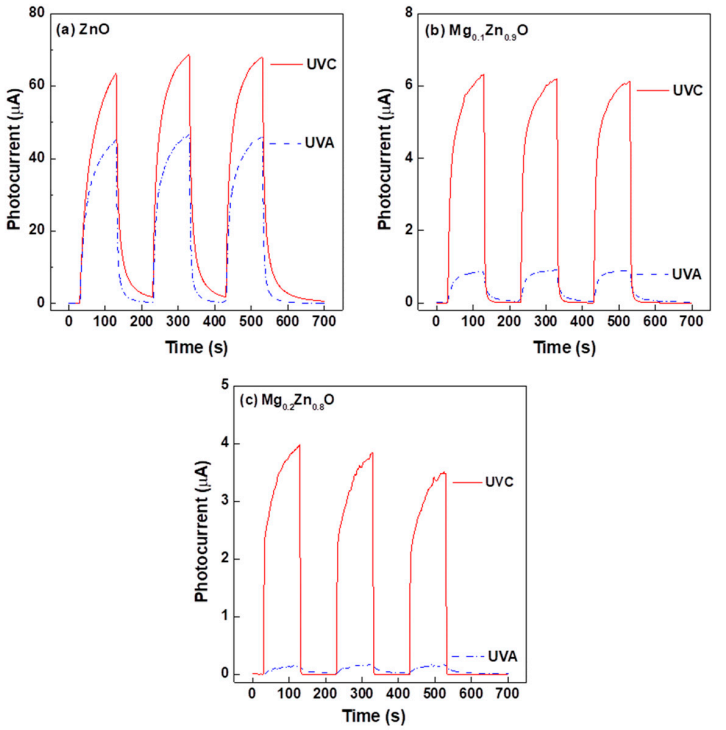

Figure 9. Time-dependent photoresponse of $Mg_xZn_{1-x}O$ photodetectors under UVA and UVC light illumination; the photodetectors had (**a**) ZnO, (**b**) $Mg_{0.1}Zn_{0.9}O$, and (**c**) $Mg_{0.2}Zn_{0.8}O$ sensing layers. The applied bias voltage in the three kinds of devices was 5 V; the period of illumination was maintained at 100 s.

Experimental results showed that the dark current and photocurrent of all thin film samples increased almost linearly with the bias voltage in the range of −5 V to 5 V (Figure 8 and Figure S4). The *I*–*V* characteristics showed a linear dependence, indicating that the MSM structured Au/$Mg_xZn_{1-x}O$/Au had an ohmic contact between Au electrodes and $Mg_xZn_{1-x}O$ semiconductor thin films and exhibited the nature of classical photoconductive devices. The measured dark currents were 1.51, 0.68, 0.31, and 0.26 nA at a 5 V bias corresponding to x = 0, 0.1, 0.2, and 0.3 samples, respectively. The dark currents of $Mg_xZn_{1-x}O$ devices were compared with the report of Yu et al. (0.5 nA) [14]. Yang et al. proposed that a low dark current level is helpful to raise the signal-to-noise ratio of the photodetector because the shot noise is proportional to the dark current [18]. It is well noted that the photocurrent induced by UVC light illumination was significantly higher than that of visible light, a feature that is helpful to achieve a high UVC-to-visible rejection ratio. According to the presented *I*–*V* characteristics, both dark currents and photocurrents of the devices at a 5 V bias decreased dramatically with increasing Mg content, which can be explained by the decrease in the electron concentration density caused by Mg substitution.

We determined the UV photoresponse (I_{UVA}/I_{dark} and I_{UVC}/I_{dark}) and UV-to-visible rejection ratio ($I_{UVA}/I_{visible}$ and $I_{UVC}/I_{visible}$) to evaluate the ability of photoelectrical conversion of a photodetector as well as the possibility that a photodetector could effectively reject the interference of visible light. Table 2 presents the UVA photoresponse, UVC photoresponse, UVA-to-visible rejection ratio, and UVC-to-visible rejection ratio. The results show that the UVA photoresponse decreased with increasing Mg content, while the UVC photoresponse was higher than 1.0×10^4; the ZnO and $Mg_{0.2}Zn_{0.8}O$ photodetectors exhibited the highest UVA-to-visible rejection ratio of 23.79 and UVC-to-visible rejection ratio of 433.3. The UVC-to-visible rejection ratio (>430) of the $Mg_{0.2}Zn_{0.8}O$ device was more than two orders of magnitude, indicating a high degree of visible blindness. Yu et al. fabricated UV photodetectors based on sol-gel derived $Mg_{0.18}Zn_{0.82}O$ nanoparticles, which exhibited UV to visible reject ratio was up to two orders of magnitude [14]. The MgZnO devices exhibited a minor photocurrent under visible light illumination due to the incident light having photon energy lower than the bandgap that excites photocarriers.

Table 2. Summary of the photoconductive properties of MSM photodetectors based on sol-gel derived $Mg_xZn_{1-x}O$ thin films.

Mg Content in $Mg_xZn_{1-x}O$ Sensing Layer		x = 0	x = 0.1	x = 0.2
UVA	UVA photoresponse (I_{UVA}/I_{dark})	3.01×10^4	1.29×10^3	7.02×10^2
	UVA-to-visible rejection ratio ($I_{UVA}/I_{visible}$)	23.79	4.60	14.94
	photoconductivity gain (I_{on}/I_{off})	534.4	43.62	29.08
	Percentage of sensitivity ((I_{ph}/I_{off}) ×100)	53,340	4262	2808
	Responsivity (I_{ph}/P_{opt}) in mA/W	379.7	7.173	1.176
UVC	UVC photoresponse (I_{UVC}/I_{dark})	8.95×10^4	1.21×10^4	2.04×10^4
	UVC-to-visible rejection ratio ($I_{UVC}/I_{visible}$)	70.82	43.18	433.3
	photoconductivity gain (I_{on}/I_{off})	345.0	5401	2216
	Percentage of sensitivity ((I_{ph}/I_{off}) ×100)	34,405	540,003	221,489
	Responsivity (I_{ph}/P_{opt}) in mA/W	198.3	19.73	12.45

It has been proposed that an interaction mechanism for oxygen molecules from air adsorbed on the ZnO surface can explain the sensitivity characteristics of photoconductive detectors [38]. In the dark state (without light illumination), oxygen molecules are absorbed by capturing free electrons from ZnO-based thin films, creating electron depletion zones near the surface and reducing the conductivity. When the films are exposed to solar light, electron-hole pairs are generated by absorption of photons. After that, holes will recombine with electrons adsorbed by oxygen ions, and that action will release oxygen molecules back into the air. The photo-generated electrons contribute to the increased carrier concentration and enhance conductivity.

Due to the low electron concentration density (~2.51 × 10^{13} cm^{-3}), the time-dependent photoresponse of the $Mg_{0.3}Zn_{0.7}O$ photodetectors was not measurable in this study. Moreover, with these as-synthesized $Mg_xZn_{1-x}O$ thin films, a photogenerated current was hard to detect for wavelengths of light longer than 400 nm because their bandgap energies were higher than 3.25 eV. Figure 9 shows the time-dependent photoresponse characteristics of ZnO, $Mg_{0.1}Zn_{0.9}O$, and $Mg_{0.2}Zn_{0.8}O$ photodetectors under periodic UVA and UVC light illumination at a fixed bias of 5 V with an interval time of 100 s, revealing good periodic repeatability and reproducibility.

Similar photoresponse behaviors were found in the three kinds of photodetectors. The recorded photocurrent versus exposure time (*I*–*T*) curves exhibited an almost sail-like shape under UV light illumination because the photocurrent increased rapidly with exposure time and achieved a specific saturation level, giving I_{on} (indicating an on current). This was due to the increase of electrical conductivity of the oxide semiconductors due to the generation of photocarriers when UV light with photo energy greater than the bandgap energy was absorbed. In a semiconductor photodetector, the generation of photocurrent involves two steps: (1) photo−generation of carriers and (2) the carrier transportation from one electrode to the other [23]. When the UV light was turned off, the photocurrent significantly decreased and tended to return to its original current level, giving I_{off} (indicating an off current). It has been reported that the MSM UV photodetector based on sol-gel derived ZnO thin film exhibits slower response and recovery speeds at room temperature, a feature that can be ascribed to the presence of defect states within the forbidden band of the polycrystalline ZnO semiconductor thin films [34,39].

The photoconductivity gain, percentage of sensitivity, and responsivity are crucial parameters for evaluating and quantifying the performance of a photodetector [6,40]. The photoconductivity gain (*K*) is defined as the ratio of on current (I_{on}) per off current (I_{off}) and is expressed as:

$$K = I_{on}/I_{off} \quad (4)$$

Percentage of sensitivity (*S*) is defined as the ratio of generated photocurrent ($I_{ph} = I_{on} - I_{off}$) per off current ($I_{off}$), given as follows:

$$S = I_{ph}/I_{off} \quad (5)$$

The responsivity (*R*) is defined as the photocurrent (I_{ph}) per unit of incident optical power (P_{opt}) and is described as follows:

$$R = I_{ph}/P_{opt} \quad (6)$$

The calculated results of three photosensing parameters for the ZnO, $Mg_{0.1}Zn_{0.9}O$, and $Mg_{0.2}Zn_{0.8}O$ photodetectors under UVA and UVC illumination are summarized in Table 2. We found that the pure ZnO photodetector exhibited the best photoconductivity gain, percentage of sensitivity, and responsivity under UVA illumination, and that the performance of $Mg_xZn_{1-x}O$ photodetectors was degraded with increasing Mg content due to bandgap energy widening and electrical barrier increasing. Under UVC illumination, the photoconductivity gain and percentage of sensitivity of the two MgZnO photodetectors were better than those of the pure ZnO photodetector and the $Mg_{0.1}Zn_{0.9}O$ device had the best photoconductivity gain of 5401 and percentage of sensitivity of 540,003. In addition, the responsivities of the three $Mg_xZn_{1-x}O$ photodetectors were 198.3, 19.73, and 12.45 mA/W corresponding to x = 0, 0.1, and 0.2 devices, respectively. Responsivity is strongly related to the measured photocurrent (Equation (6)). High responsivity can be ascribed to high photocurrent due to many more photo-generated carriers being collected under illumination. Table 3 listed previous results of UV photodetectors with sol-gel derived ZnO or MgZnO sensing layer. Fang et al. reported that the responsivity of most commercial UV photodetectors was in the range of 0.1–0.2 A/W [41]. Experimental results indicated that the sol-gel synthesized nanocrystalline $Mg_{0.1}Zn_{0.9}O$ semiconductor thin film is a possible candidate for fabrication of solar-blind photodetectors after improving the responsivity.

Table 3. Comparison of results of different sol-gel derived UV photodetectors.

Sensing Material	Substrate	Annealing Temperature (°C)	Responsivity (mA/W)	Peak Wavelength	Reference
ZnO	sapphire	550	40	350 nm	[34]
$Mg_{0.2}Zn_{0.8}O$	quartz	900	550	336 nm	[13]
$Mg_{0.02}Zn_{0.98}O$/ZnO	glass	450	165	356 nm	[15]
$Mg_{0.18}Zn_{0.82}O$	quartz	600	270	322 nm	[14]
ZnO	glass	500	~ 200	UVC	This work
$Mg_{0.1}Zn_{0.9}O$	glass	500	~ 20	UVC	This work

4. Conclusions

Device-quality $Mg_xZn_{1-x}O$ transparent semiconductor thin films were fabricated on glass substrates by sol-gel spin-coating process, and their application was realized in visible-blind, ultraviolet-sensitive photoconductive detectors with a simple MSM structure. The as-prepared ZnO-based thin films had a single-phase wurtzite structure, and the average crystallite size of the films was in the range of 18.3–13.0 nm varied with Mg content. The optical transmittance of the MgZnO thin films was higher than 92% in the visible region. The widening of the optical bandgap energy of the $Mg_xZn_{1-x}O$ thin films varied with Mg content and corresponded to the blue shift of the absorption edge in the optical transmittance spectrum and UV emission peak in the PL spectrum. We demonstrated that incorporation of Mg into ZnO nanocrystals could decrease the electron concentration density. According to the *I–V* characteristics, both dark currents and photocurrents of the photodetectors decreased dramatically with increasing Mg content. The photocurrent induced by UVC light illumination was significantly higher than those induced by visible and UVA light. The time-dependent photoresponse characteristics of ZnO, $Mg_{0.1}Zn_{0.9}O$, and $Mg_{0.2}Zn_{0.8}O$ photodetectors under periodic UVA and UVC light illumination at a fixed bias of 5 V revealed good periodic repeatability and reproducibility. Under UVC illumination, the photoconductivity gain and percentage of sensitivity of the $Mg_{0.1}Zn_{0.9}O$, and $Mg_{0.2}Zn_{0.8}O$ photodetectors were better than those of the pure ZnO photodetector; the $Mg_{0.1}Zn_{0.9}O$ photodetector had the best photoconductivity gain of 5401 and percentage of sensitivity of 540,003.

Supplementary Materials: The following are available online at http://www.mdpi.com/2079-6412/9/4/277/s1, Figure S1: Top−view optical microscope (OM) image of the Au interdigitated electrodes (IDEs) of the fabricated photodetector device; Figure S2: Plane-view field-emission scanning electron microscope (FE-SEM) micrographs of $Mg_xZn_{1-x}O$ thin films on glass substrates: (a) $x = 0$, (b) $x = 0.1$, (c) $x = 0.2$, and (d) $x = 0.3$; Figure S3: Surface scanning probe microscope (SPM) images of $Mg_xZn_{1-x}O$ thin films: (a) $x = 0$ and (b) $x = 0.2$; Figure S4: Optical reflection spectra of glass/ $Mg_xZn_{1-x}O$ thin films; Figure S5: Current-voltage (*I-V*) characteristics of $Mg_{0.3}Zn_{0.7}O$ photodetectors showing dark current and photoilluminated currents under irradiation with visible, UVA and UVC light.

Author Contributions: Conceptualization, C.-Y.T.; Methodology, C.-Y.T., S.-T.C., and M.-T.F.; Validation, C.-Y.T.; Investigation and Resources, C.-Y.T.; Data Curation, C.-Y.T., S.-T.C., and M.-T.F.; Writing—Original Draft Preparation and Writing—Review and Editing, C.-Y.T.; Visualization, C.-Y.T.; Supervision, C.-Y.T.; Project Administration and Funding Acquisition, C.-Y.T.

Funding: This study received financial support from the Ministry of Science and Technology (MOST) of Taiwan under MOST No. 104-2221-E-035-009.

Acknowledgments: The authors gratefully acknowledge the Precision Instrument Support Center of Feng Chia University for providing the measurement facilities.

Conflicts of Interest: The authors declare that there is no conflict of interest regarding the publication of this paper.

References

1. Sang, L.; Liao, M.; Sumiya, M. A comprehensive review of semiconductor ultraviolet photodetectors: From thin film to one-dimensional nanostructures. *Sensors* **2013**, *13*, 10482–10518. [CrossRef]
2. Alaie, Z.; Nejad, S.M.; Yousefi, M.H. Recent advances in ultraviolet photodetectors. *Mat. Sci. Semicond. Process.* **2015**, *29*, 16–55. [CrossRef]

3. Nasiri, N.; Jin, D.; Tricoli, A. Nanoarchitechtonics of visible-blind ultraviolet photodetectors materials: Critical features and nano-microfabrication. *Adv. Opt. Mater.* **2018**, *7*, 1800580. [CrossRef]
4. Khokhra, R.; Bharti, B.; Lee, H.N.; Kumar, R. Visible and UV photo-detector in ZnO nanostructured thin films via simple tuning of solution method. *Sci. Rep.* **2017**, *7*, 15032. [CrossRef]
5. Liu, K.; Sakurai, M.; Aono, M. ZnO-based ultraviolet photodetectors. *Sensors* **2010**, *10*, 8604–8634. [CrossRef]
6. Tsay, C.Y.; Hsu, W.T. Comparative studies on ultraviolet-light derived photoresponse properties of ZnO, AZO, and GZO transparent semiconductor thin films. *Materials* **2017**, *10*, 1379. [CrossRef]
7. Syu, J.C.; Hsu, M.H.; Chang, S.P.; Chang, S.J.; Lu, L. Effect of oxygen vacancy ratio on a GaZTO solar-blind photodetector. *Coatings* **2018**, *8*, 293. [CrossRef]
8. Gondoni, P.; Ghidelli, M.; Di Fionzo, F.; Russo, V.; Bruno, P.; Marti-Rujas, J.; Bottani, C.E.; Bassi, A.L.; Casari, C.S. Structural and functional properties of Al:ZnO thin films grown by pulsed laser deposition at room temperature. *Thin Solid Films* **2012**, *520*, 4707–4711. [CrossRef]
9. Gondoni, P.; Ghidelli, M.; Di Fionzo, F.; Carminati, M.; Russo, V.; Bassi, A.L.; Casari, C.S. Structure-dependent optical and electrical transport properties of nanostructured Al-doped ZnO. *Nanotechnology* **2012**, *23*, 365706. [CrossRef]
10. Kaushal, A.; Kaur, D. Effect of Mg content on structural, electrical and optical properties of $Zn_{1-x}Mg_xO$ nanocomposite thin films. *Sol. Energy Mater. Sol. Cells* **2009**, *93*, 193–198. [CrossRef]
11. Wang, X.; Saito, K.; Tanaka, T.; Nishio, M.; Nagaka, T.; Arita, M.; Guo, Q. Energy band bowing parameter in MgZnO alloys. *Appl. Phys. Lett.* **2015**, *107*, 022111. [CrossRef]
12. Hou, Y.; Mei, Z.; Du, X. Semiconductor ultraviolet photodetectors based on ZnO and $Mg_xZn_{1-x}O$. *J. Phys. D Appl. Phys.* **2014**, *47*, 283001. [CrossRef]
13. Liu, H.; Liu, Q.; Ma, X.; Wang, H.; Zang, M.; Zhang, X. Synthesis and photoelectrical properties of nanometer size $Mg_{0.2}Zn_{0.8}O$ films. *Mater. Sci. Semicond. Process.* **2018**, *74*, 199–202. [CrossRef]
14. Yu, J.; Tian, N.; Deng, Y.F.; Zhang, H.H. Ultraviolet photodetectors based on sol-gel synthesized MgZnO thin film nanoparticle with photoconductive gain. *J. Alloy. Compd.* **2016**, *667*, 359–362. [CrossRef]
15. Rana, V.S.; Rajput, J.K.; Pathak, T.K.; Purohit, L.P. Multilayer MgZnO/ZnO thin films for UV photodetectors. *J. Alloy. Compd.* **2018**, *764*, 724–729. [CrossRef]
16. Shiau, J.S.; Brahma, S.; Liu, C.P.; Huang, J.L. Ultraviolet photodetectors based on MgZnO thin film grown by RF magnetron sputtering. *Thin Solid Films* **2016**, *620*, 170–174. [CrossRef]
17. Jiang, D.Y.; Zhang, J.Y.; Liu, K.W.; Zhao, Y.M.; Cong, C.X.; Lu, Y.M.; Yao, B.; Zhang, Z.Z.; Shen, D.Z. A high-speed photoconductive UV detector based on an $Mg_{0.4}Zn_{0.6}O$ thin film. *Semicond. Sci. Technol.* **2007**, *22*, 687. [CrossRef]
18. Yang, W.; Vispute, R.D.; Choopun, S.; Sharma, R.P.; Venkatesan, T.; Shen, H. Ultraviolet photoconductive detector based on epitaxial $Mg_{0.34}Zn_{0.66}O$ thin films. *Appl. Phys. Lett.* **2001**, *78*, 2787–2789. [CrossRef]
19. Ohtomo, A.; Kawasaki, M.; Koida, T.; Masubuchi, K.; Koinuma, H.; Sakurai, Y.; Yoshida, Y.; Yasuda, T.; Segawa, Y. $Mg_xZn_{1-x}O$ as a II-IV widegap semiconductor alloy. *Appl. Phys. Lett.* **1998**, *72*, 2466–2468. [CrossRef]
20. Huang, K.; Tang, Z.; Zhang, L.; Yu, J.; Lv, J.; Liu, X.; Liu, F. Preparation and characterization of Mg-doped ZnO thin films by sol-gel methods. *Appl. Surf. Sci.* **2012**, *258*, 3710–3713. [CrossRef]
21. Wang, M.; Kim, E.J.; Kim, S.; Chung, J.S.; Yoo, I.K.; Shin, E.W.; Hahn, S.H.; Park, C. Optical and structural properties of sol-gel prepared MgZnO alloy thin films. *Thin Solid Films* **2008**, *516*, 1124–1129. [CrossRef]
22. Garcia de Arquer, F.P.; Armin, A.; Meredith, P.; Sargent, E.H. Solution-processed semiconductors for next-generation photodetectors. *Nat. Rev. Mater.* **2017**, *2*, 16100. [CrossRef]
23. Zhang, K.; Yang, Z.; Wang, M.; Cao, M.; Sun, Z.; Shao, J. Low temperature annealed ZnO film UV photodetector with fast photoresponse. *Sens. Actuat. A* **2017**, *253*, 173–180. [CrossRef]
24. Zak, A.K.; Majid, W.A.; Abrishami, M.E.; Yousefi, R. X-ray analysis of ZnO nanoparticles by Williamson-Hall and size-strain plot methods. *Solid State Sci.* **2011**, *13*, 251–256. [CrossRef]
25. Singh, S.K.; Hazra, P. Performance analysis of undoped and Mg-doepd ZnO/p-Si heterojunction diodes grown by sol-gel technique. *J. Mater. Sci. Mater. Electron.* **2018**, *29*, 5213–5223. [CrossRef]
26. Mahroug, A.; Mari, B.; Mollar, M.; Boudjadar, I.; Guerbous, L.; Henni, A.; Selmi, N. Studies on structural, surface morphological, optical, luminescence and UV photodetection properties of sol-gel Mg-doped ZnO thin films. *Surf. Rev. Lett.* **2018**, *26*, 1850167. [CrossRef]

27. Tsay, C.Y.; Wang, M.C.; Chiang, S.C. Effects of Mg additions on microstructure and optical properties of sol-gel derived ZnO thin films. *Mater. Trans.* **2008**, *49*, 1186–1191. [CrossRef]
28. Kim, Y.S.; Tai, W.P. Electrical and optical properties of Al-doped ZnO thin films by sol-gel process. *Appl. Surf. Sci.* **2007**, *253*, 4911–4916. [CrossRef]
29. Arshad, M.; Ansari, M.M.; Ahmed, A.S.; Tripathi, P.; Ashraf, S.S.Z.; Naqvi, A.H.; Azam, A. Band gap engineering and enhanced photoluminescence of Mg doped ZnO nanoparticles synthesized by wet chemical route. *J. Lumin.* **2015**, *161*, 275–280. [CrossRef]
30. Singh, A.; Vij, A.; Kumar, D.; Khanna, P.K.; Kumar, M.; Gautam, S.; Chae, K.H. Investigated of phase segregation in sol-gel derived ZnMgO thin films. *Semicond. Sci. Technol.* **2013**, *28*, 025004. [CrossRef]
31. Sonawane, B.K.; Bhole, M.P.; Patil, D.S. Structural, optical and electrical properties of $Mg_xZn_{1-x}O$. *Mater. Sci. Semicond. Process.* **2009**, *12*, 212–216. [CrossRef]
32. Mia, M.N.H.; Pervez, M.F.; Hossain, M.K.; Rahman, M.R.; Uddin, M.J.; Al Mashud, M.A.; Ghosh, H.K.; Hoq, M. Influence of Mg content on tailoring optical bandgap of Mg-doped ZnO thin film prepared by sol-gel method. *Results Phys.* **2017**, *7*, 2683–2691. [CrossRef]
33. Ai, Q.; Liu, K.; Ma, H.; Yang, J.; Chen, X.; Li, B.; Shen, D. Ultraviolet electroluminescence from a *n*-ZnO film/p-GaN heterojunction under both forward and reverse bias. *J. Mater. Chem. C* **2018**, *6*, 11368–11373. [CrossRef]
34. Basak, D.; Amin, G.; Mallik, B.; Paul, G.K.; Sen, S.K. Photoconductive UV detectors on sol-gel-synthesized ZnO films. *J. Cryst. Growth* **2003**, *256*, 73–77. [CrossRef]
35. Ogawa, Y.; Fujihara, S. Band-gap modification and tunable blue luminescence of wurtzite $Mg_xZn_{1-x}O$ thin films. *Phys. Status Solidi (a)* **2005**, *202*, 1825–1828. [CrossRef]
36. Fujihara, S.; Sasaki, C.; Kimura, T. Effects of Li and Mg doping on microstructure and properties of sol-gel ZnO thin films. *J. Eur. Ceram. Soc.* **2001**, *21*, 2109–2112. [CrossRef]
37. Cohen, D.J.; Ruthe, K.C.; Barnett, S.A. Transparent conducting $Zn_{1-x}Mg_xO$:(Al,In) thin films. *J. Appl. Phys.* **2004**, *96*, 459–467. [CrossRef]
38. Salah, M.; Azizi, S.; Boukhachem, A.; Khaldi, C.; Amlouk, M.; Lamloumi, J. Structural, morphological, optical and photodetector properties of sprayed Li-doped ZnO thin films. *J. Mater. Sci.* **2017**, *52*, 10439–10454. [CrossRef]
39. Yang, Z.; Wang, M.; Ding, J.; Sun, Z.; Li, L.; Huang, J.; Liu, J.; Shao, J. Semi-transparent ZnO-CuI/CuSCN photodiode detector with narrow-band UV photoresponse. *ACS Appl. Mater. Interfaces* **2015**, *7*, 21235–21244. [CrossRef]
40. Saravanakumar, B.; Mohan, R.; Thiyagarajan, K.; Kim, S.J. Investigation of UV photoresponse property of Al, N co-doped ZnO film. *J. Alloy. Compd.* **2013**, *580*, 538–543. [CrossRef]
41. Fang, F.; Futter, J.; Markwitz, A.; Kennedy, J. UV and humidity sensing properties of ZnO nanorods prepared by the arc discharge method. *Nanotechnology* **2009**, *20*, 245502. [CrossRef]